Catalysis Today xxx (xxxx) xxx–xxx

Contents lists available at ScienceDirect

Catalysis Today

journal homepage: www.elsevier.com/locate/cattod

# A comprehensive review on wettability, desalination, and purification using graphene-based materials at water interfaces

Seongpil An[a,1], Bhavana N. Joshi[a,1], Jong-Gun Lee[a,1], Min Wook Lee[b], Yong Il Kim[a], Min-woo Kim[a], Hong Seok Jo[a], Sam S. Yoon[a,*]

[a] School of Mechanical Engineering, Korea University, Seoul 02841, Republic of Korea
[b] Department of Mechanical and Industrial Engineering, University of Illinois at Chicago, 842 W. Taylor St., Chicago, IL 60607-7022, USA

ARTICLE INFO

*Keywords:*
Graphene
Wettability
Desalination
Purification

ABSTRACT

Graphene has several outstanding properties that make it suitable for use in a wide range of electronic devices and applications. Although the use of graphene has led to considerable increases in the performance of such devices, recent global concerns regarding water pollution have necessitated studies on graphene as a green material. The fact that graphene shows unique wetting characteristics and has a carbon-based porous structure suggests it should hold great promise for use in water desalination and purification. Thus, understanding the behavior of water at graphene interfaces is necessary for further enhancements in the desalination and purification processes. Hence, this review focuses on the recent advances made in these research areas, while considering the wettability of graphene, and aims to provide insights into the development of graphene-based water desalination and purification technologies.

## 1. Introduction

Graphene, a two-dimensional (2D) structured sheet consisting of $sp^2$-hybridized carbon atoms, has attracted great attention because it possesses outstanding mechanical, electrochemical, and thermal properties [1–4]. For example, ideal monolayered graphene has an ultrahigh specific surface area (2630 $m^2\,g^{-1}$) and shows an electron mobility of $2.5 \times 10^5\,cm^2\,V^{-1}\,S^{-1}$ and thermal conductivity of $5000\,W\,m\,K^{-1}$ [5]. Recently, with the development of methods for high-yield graphene production [6–9], there has been an exponential increase in the number of studies on graphene as an advanced material [10]. These studies have contributed to technological advances in various engineering fields. Thus, graphene research is expected to continue to increase in the future.

However, despite these developments, recent studies on graphene have mostly concentrated on its use in electronic devices and applications, such as high-speed electronics [11], data storage devices [12], displays [13], batteries [14], solar cells [15], and sensors [16]. Even though advancements in state-of-the-art electronics are essential for human development, graphene may be more useful to humans as an environmental material.

With concerns about water pollution growing all over the world in recent decades, finding new materials and technologies for water desalination (WD) and purification has become imperative. With the world population growing exponentially, the demand for drinking water has also increased dramatically. Thus, the issue of desalination has become an even more urgent one. Further, while these is a pressing need for advanced desalination technologies, the flow of hazardous wastewater from manufacturing and farming industries has become a threat to humans and the environment. This has increased the urgency of developing advanced purification technologies. Thus, economically feasible and scalable technologies for the desalination and purification of water need to be implemented not only for recycling water but also to protect humans from illnesses and the environment from the damage caused by the pollutants.

In this review, the potential of graphene-based materials for use in desalination and purification technologies is discussed, because such materials have extraordinary properties and can result in significant improvements in the desalination and purification of water.

## 2. Wettability of graphene

Because graphene is considered one of the most attractive coating materials discovered in recent decades [17–20], a deep understanding of its wettability properties is essential, in order to be able to use it in various applications, including in membranes [21,22], batteries

* Corresponding author.
*E-mail address:* skyoon@korea.ac.kr (S.S. Yoon).
[1] These authors contributed equally to this work.

http://dx.doi.org/10.1016/j.cattod.2017.04.027
Received 19 December 2016; Received in revised form 24 March 2017; Accepted 13 April 2017
0920-5861/ © 2017 Elsevier B.V. All rights reserved.

[23–25], and cooling materials [26,27]. Accordingly, several recent studies have examined the effects of graphene wettability on its electronic and thermal performance. This has led to improvements in the energy-storage capacity and heat-transfer coefficient of the material [25,28]. Deep insights into the wettability of graphene will not only provide an understanding of the properties of graphene–liquid interfaces but should also result in improvements in the performance of graphene-based devices.

Depending on the range of water contact angles (WCAs) exhibited by a material, it can be classified as superhydrophilic, hydrophilic, hydrophobic, or superhydrophobic. The WCA of a hydrophilic surface ranges from 0 to 90°, whereas that of a hydrophobic surface ranges from 90 to 180° [29]. In particular, a surface with an extremely low WCA (~0°), which indicates a high surface energy, is considered superhydrophilic; conversely, a surface with an ultrahigh WCA (above 150°) is deemed superhydrophobic [30].

WCA measurements have been a popular method of evaluating the wettability properties of materials since Young introduced the following equation, which is called Young's equation [31]:

$$\gamma_{SG} - \gamma_{SL} - \gamma_{LG} \cos\theta = 0 \quad (1)$$

where $\theta$ is the contact angle (°) and $\gamma_{SG}$, $\gamma_{SL}$, and $\gamma_{LG}$ are the surface energies of the solid–vapor, solid–liquid, and liquid–vapor interfaces, respectively (Fig. 1a). However, Young's equation is applicable only for perfectly flat and rigid surfaces, often called ideal surfaces; this limits its use in the case of actual surfaces, which are usually rough. To better elucidate the wettability of nonideal real surfaces as a function of the surface roughness, the Wenzel and Cassie–Baxter models can be used for homogeneous and heterogeneous surfaces, respectively [32,33]; these models are described by the equations given below. Note that homogeneous surfaces correspond to the case where water (or the liquid in question) adheres completely to the rough surface, and no trapped air is present (Fig. 1b). On the other hand, it is assumed that a considerable amount of air is trapped between the water (or liquid) and the textured surface in case of heterogeneous surfaces (Fig. 1c).

$$\cos\theta_{rough} = r \cos\theta_{flat} \quad (2)$$

where $\theta_{rough}$ and $\theta_{flat}$ are the WCAs of the rough and flat surfaces, respectively. Note that the $\theta_{flat}$ value is based on the assumption that the flat surface is composed of the same components as the rough surface. The roughness factor, $r$, is defined as the ratio of the actual surface area to the projected surface area; thus, the $r$ value is always greater than 1. Accordingly, the Wenzel equation (Eq. (2)) suggests that increases in the roughness of hydrophilic ($0° < \theta_{flat} < 90°$) and hydrophobic ($90° < \theta_{flat} < 180°$) surfaces result in increased hydrophilicity and hydrophobicity, respectively.

$$\cos\theta_{rough} = f_1 \cos\theta_1 + f_2 \cos\theta_2 \quad (3)$$

In the Cassie–Baxter equation (Eq. (3)), $f_1$ and $f_2$ are the area fractions of the water and air phases, respectively, and $\theta_1$ and $\theta_2$ are the corresponding contact angles. Because air is trapped at the interface in the case of a heterogeneous surface, the contact angle of air is $\theta_2 = 180°$. Thus, Eq. (3) can be simplified as

$$\cos\theta_{rough} = f_1 \cos\theta_1 - f_2 \quad (4)$$

This indicates that $\theta_{rough}$ increases with an increase in $f_2$. That is to say, the microsized air bubbles attributable to the rough surface make the surface even more superhydrophobic. Hence, several studies on superhydrophobic surfaces have used the Cassie–Baxter model [34–38].

### 2.1. Intrinsic wettability of graphene

In contrast to the conventional belief that graphene is a hydrophobic material [39–42], it was recently claimed that graphene is hydrophilic and exhibits a low WCA (45°) [43–47]. According to these studies, the known hydrophobicity of the graphene is attributable to the inadvertent accumulation of hydrocarbons on its surface. Ashraf et al. [44] reported that early-stage WCA measurements of multilayered graphene indicate that it is hydrophilic whereas WCA measurements performed after exposures of 30 s, 1 min, and 1 day to the atmosphere showed that the WCA increases by up to 10°, 20°, and 40°, respectively, owing to the hydrocarbons present on the surface. Although the wettability of graphene remains a topic of debate because of these contradictory findings, the effect of airborne contaminants on the wettability transition seems quite clear [48–50]. For example, Arial et al. [50] showed experimentally that the WCA of graphene, which ranged initially from 61° to 85°, increased to 98° after prolonged exposure to air (Fig. 2). X-ray photoelectron spectroscopy (XPS) measurements revealed that airborne contaminants were adsorbed onto the graphene surface, resulting in a decrease in the surface energy by 10–16%.

However, it should be emphasized that most graphene samples that meet industrial standards show hydrophobicity [29,51–53]. This is because most fabrication methods that are economically viable and industrially scalable inevitably induce defects and wrinkles in the fabricated graphene, thus causing hydrocarbon contamination, which results in heterogeneous air-embedding graphene structures. For this reason, most studies on the applications of graphene have focused on its hydrophobic properties. In particular, the production of superhydrophobic graphene by structural and chemical modification techniques has attracted considerable attention with respect to specific applications, including self-cleaning, antifouling, and sensing [54–57]. Thus, in this review, we highlight some of the methods available for obtaining superhydrophobic graphene (see Section 2.3).

### 2.2. Wetting transparency of graphene

Before one can examine the superhydrophobicity of graphene, it is essential to elucidate one of its intrinsic properties. Rafiee et al. [28] reported that monolayered graphene deposited onto copper, gold, or silicon exhibits the wettability of the underlying metal substrate. This phenomenon of so-called "wetting transparency" is possible because of long-range van der Waals forces, which are active over distances of 5 nm (Fig. 3a). According to the wetting transparency theory, the other properties (i.e., electrical conductivity and thermal conductivity, among others) of the graphene-coated metal surfaces can be varied without changing their initial values. Similarly, Shih et al. [58,59] stated that monolayered graphene shows incomplete wetting transparency. For example, it exhibits wetting transparency on hydrophilic

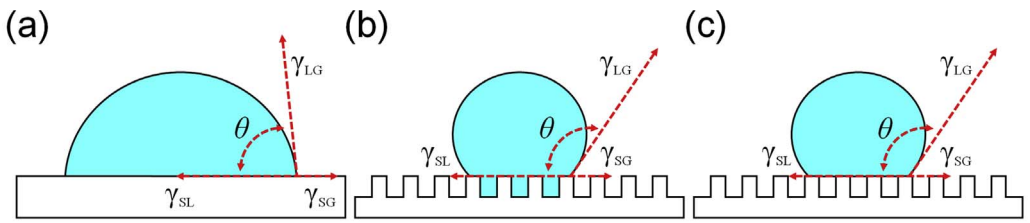


**Fig. 1.** Schematics of a water droplet on (a) flat and (b, c) rough surfaces, showing the balancing surface energies of Young's equation and the Wenzel and Cassie–Baxter models, respectively.

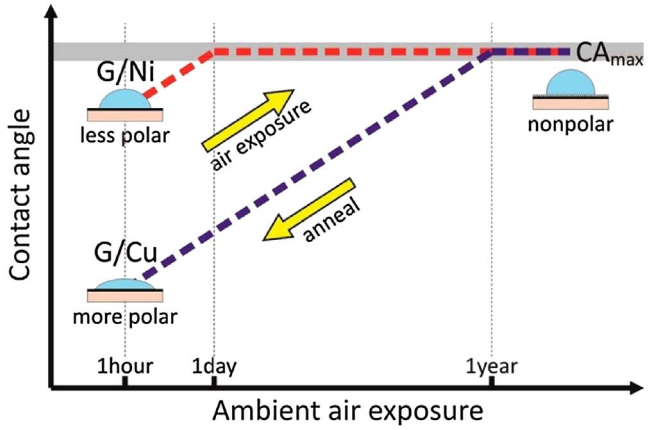


**Fig. 2.** WCA versus time of air exposure. Reprinted with permission from Ref. [50].

substrates but nonwetting transparency on hydrophobic substrates.

More recently, Raj et al. [60] reported results that contradict those described above, stating that monolayered graphene exhibits complete nonwetting transparency. They found that monolayered graphene shows a high degree of contact angle hysteresis for angles of 16–37° (Fig. 3b). In particular, the increase in the contact angle of monolayered graphene was similar to that in the contact angle of highly ordered pyrolytic graphite. This was indicative of the nonwetting transparency of graphene. They attributed this finding to the large interlayer spacing between the graphene and the underlying substrate.

These mutually incompatible findings, which may originate from differences in the experimental conditions (such as the methods used to fabricate the graphene samples used and laboratory humidity and temperature conditions [44,50,61–63]), highlight the need for further studies on the intrinsic nature of graphene.

### 2.3. Enhanced hydrophobicity of graphene

Many current studies on the superhydrophobicity of materials have focused on the phenomenon of self-cleaning [36–38,55,64], often referred to as the "lotus effect" [65], because water drops naturally roll off the surfaces of lotus leaves while attracting dirty particles, resulting in the cleaning of the leaves. The uniquely roughened surface of the lotus leaf induces the Cassie–Baxter effect, which significantly reduces the adhesion between the water droplets and the leaf surface. Inspired by this natural phenomenon, numerous researchers have studied novel materials and methods of increasing the specific surface area of materials, which would allow their surface to hold more superjacent air, or of improving their hydrophobicity. Among the various materials being investigated, carbon-based micro- and nanomaterials, including carbon nanotubes (CNTs) [66,67], carbon nanofibers [68,69], and graphene [29,70], have attracted particular interest not only for their high specific surface areas at the micro- and nanoscales but also owing to their other desirable properties. In particular, because most available graphene shows hydrophobicity (cf. Section 2.1), which is ideal for achieving superhydrophobicity, pristine graphene has recently been modified using several different techniques.

#### 2.3.1. Structural modification of graphene

One of the most widely used methods for modifying graphene to achieve a highly superhydrophobic surface is to combine it with other materials or to use several fabrication processes in combination to produce it. Such hybrid approaches aim to structurally form micro- or nanoscale pores or to chemically strengthen the hydrophobic functional groups. For example, Zha et al. [54] fabricated a hybrid polyvinylidene fluoride/graphene gel by combining the solvent exchange and freeze-drying methods. This novel approach prevents the top surface of the hybrid gel from forming a dense skin-like layer, which results in a surface with microscale roughness. Furthermore, the addition of graphene to the hybrid gel causes the overall morphology of the gel to be nanostructured to a greater degree. Consequently, this hierarchical micro- and nanoscale morphology results in an ultrahigh WCA of 153° (Table 1).

Singh et al. [55] reported a method for fabricating foam-shaped superhydrophobic graphene. The microporous graphene foam was obtained by template-directed chemical vapor deposition (CVD) and had an average pore size of 200 nm. The graphene foam not only exhibited a high (advancing) WCA (163°) (Table 1) but also showed good mechanical flexibility and durability. Thus, its suitability as a self-cleaning and antifouling material was evaluated.

More recently, Jiang et al. [70] fabricated periodically structured superhydrophobic graphene films, bioinspired by butterfly wings. Such biomimetic materials have attracted significant attention in various engineering fields. They employed a bioinspired fabrication method to create microstructured graphene films. For this, they subjected graphene oxide (GO) films to a two-beam laser interference treatment, in order to remove the oxygen-containing groups (OCGs) from the surface.

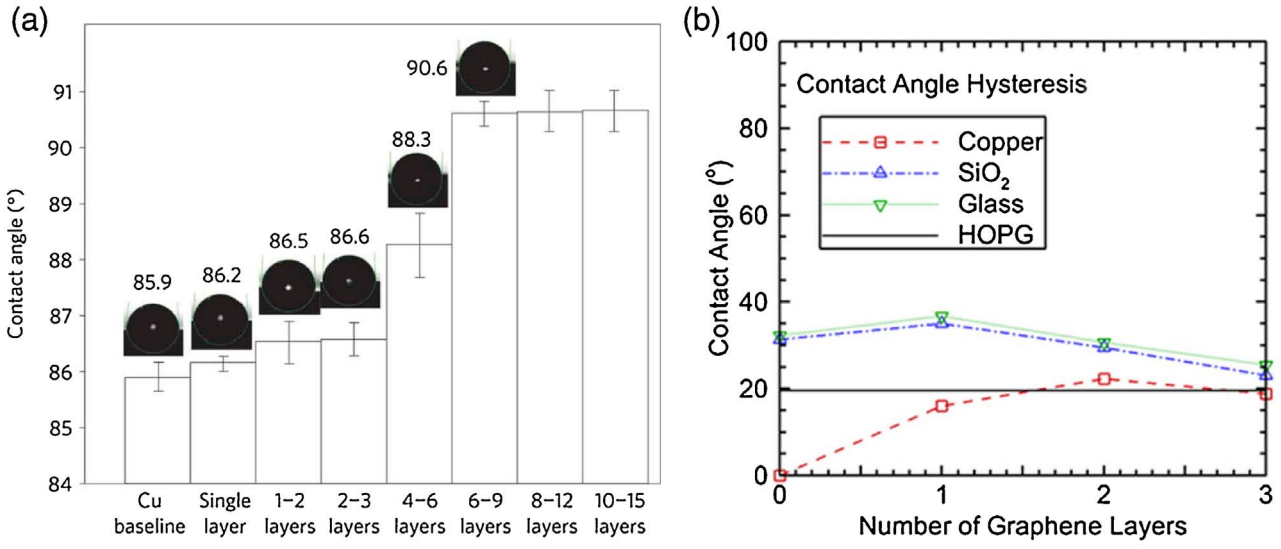


**Fig. 3.** (a) WCA on Cu substrates as a function of the number of graphene layers. Reprinted with permission from Ref. [28]. (b) WCA hysteresis as a function of the number of graphene layers on different substrates. Reprinted with permission from Ref. [60]. Copyright 2013 American Chemical Society.

**Table 1**
Modifications for superhydrophobic graphenes and corresponding WCA values.

| Type | | Water contact angle [°] | Ref |
|---|---|---|---|
| Structural modification | Polyvinylidene fluoride (PVDF)/graphene | 153 | [54] |
| | Teflon-coated 3D graphene foam | 143–163 | [55] |
| | 2D Grating-like structure | 155 | [70] |
| Chemical modification | Octadecylamine-unctionalized GO Film | 163 | [71] |
| | Perfluorodecyl-trichlorosilane (FDTS)-treated GA | 160 | [29] |

This yielded a 2D grating-like structure with a high WCA (155°) (Table 1).

### 2.3.2. Chemical modification of graphene

In addition to being subjected to structural modifications, graphene has been modified via chemical methods, with the aim of enhancing its hydrophobicity, as can be seen from Table 1. Lin et al. [71] reported a facile method for synthesizing superhydrophobic GO films; the method involved the chemical grafting of octadecylamine (ODA) onto GO sheets. ODA, which consists of long hydrocarbon chains, reduced the surface energy of the GO films, owing to which they exhibited a WCA as high as 163.2°, as well as a low degree of hysteresis (3.1°). It should be noted that chemical modifications are often combined with structural modifications.

Recently, Lin et al. [29] fabricated a novel superhydrophobic graphene aerogel (GA) using a chemical surface modification method. Aerogels are considered among the most fascinating superhydrophobic materials because of their high porosity and low density and are usually derived from silica sources. However, a recently developed GA [72] has attracted significant attention because it shows a high specific surface area as well as an inherently high electrical conductivity. Lin et al. found that the pristine GA sample showed a WCA of 135°; however, a chemical treatment with a fluorinated silane increased the WCA to 160°. Thus, the use of GAs is expected to steadily increase in the future, because GA fabrication methods are scalable, inexpensive, and simple to execute.

## 3. Desalination

Desalination is the process of removing salt from saltwater to obtain clean and potable water [73]. The natural cycle of the evaporation of ocean water is an example of desalination. Human-driven desalination processes can be classified as 1) thermal and 2) membrane based. Membrane-based techniques are cost effective and thus used more widely for WD. Typically, polymeric materials are used for making the separation membranes; however, these membranes often show poor performance [74], require the use of large amounts of energy, and have low flux permeation rates. With respect to desalination, the membrane pores play a critical role and must be small enough (< 1 nm) to reject the salt ions while allowing the water molecules to pass. The flux permeation rate is inversely proportional to the membrane thickness. In addition, the presence of hydrophilic hydroxyl groups on the surface of the membrane or within the pores improves water permeation [75]. Thus, the paradigm of WD is based on the use of thin membranes with nanopores, as they ensure a high flux and good ion selectivity [76].

### 3.1. Nanoporous graphene membranes (nanoporous filtration)

Graphene, being a 2D sheet-like material, is ultimately a thin membrane. However, it is impermeable to liquids and gases because the electron densities of its aromatic rings prevent atoms and molecules from passing through the rings. Despite this limitation, nanoporous graphene materials have being explored for use in WD because they show low fouling, high chemical resistance, good mechanical durability, high selectivity, and fast molecular transport [74,77,78]. Graphene with good mechanical strength can be manufactured on a large scale via roll-to-roll production. Nanoporous graphene and GO stacks are often used for desalination purposes [79], as shown in Fig. 4. The mechanism of WD via graphene-based membranes is depicted in Fig. 4. The nanoporous graphene rejects the salt because of the large sizes of the ions as well as owing to electrostatic interactions, whereas in the case of GO, ion adsorption also results in salt rejection. Water permeation is higher in stacked GO membranes because of the 2D nanochannels that are formed as well as owing to low friction.

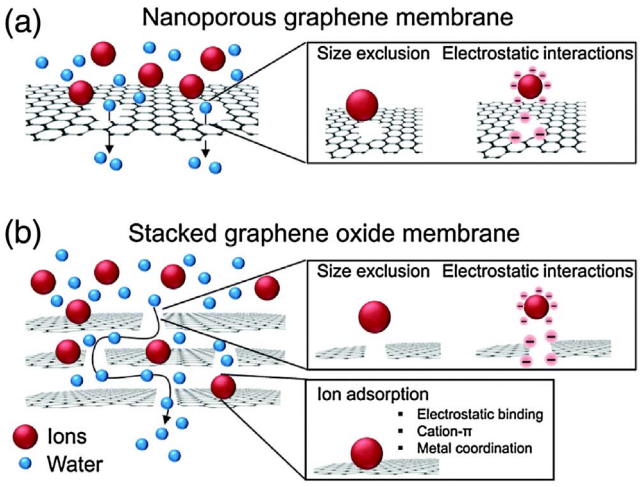


**Fig. 4.** (a) Nanoporous graphene membrane and (b) stacked GO membrane for WD. Reprinted with permission from Ref. [79] with permission of The Royal Society of Chemistry.

### 3.1.1. Simulation studies

Using computations, Cohen-Tanugi et al. [80] showed that the hydroxyl groups on nanoporous graphene materials with suitable pores block salt ions. In addition, the water flux rate is also very high. As a result, the water permeability of such graphene materials is much higher than that of the conventional membranes used for reverse-osmosis. However, the presence of pores weakens the graphene by reducing its fracture strength. During the WD process, the membrane remains wet and is subjected to stresses that exceed the limit placed by its thickness. A systematic simulation study on the mechanical strength of nanoporous graphene by Cohen-Tanugi et al. suggested that using substrates having pores smaller than 1 μm would allow graphene to withstand pressures as high as 570 bar [81]. The selective passage of ions through nanoporous graphene is determined by the pore size, electrostatic interactions between the ions and pores, and pore functionalization [74,82]. Simulation studies have shown that hydrophilic pores result in a higher water flux but lower salt rejection rate than is the case for hydrophobic pores. Thus, the functionalization of the pores with $COO^-$ and $NH_3^+$ improves their ability to reject NaCl [83]. Simulation models of functionalized pores are presented in Fig. 5. Using molecular dynamics (MD) simulations, Ang et al. [84] recently studied freestanding and frozen graphene membranes for salt rejection; the modeled graphene membrane had circular pores with a diameter of 0.5 nm or slits with a length of 0.228 nm. The slits in the graphene sheet were modeled as being perpendicular to the transport direction. Compared to the membrane with circular pores, the slit-containing membrane exhibited improved salt rejection and water permeation performances. A similar slit-containing membrane was also investigated by Muscatello et al. [85]. Similarly, using MD simulations, Azmat [86] studied the WD performance of graphene with functionalized pores

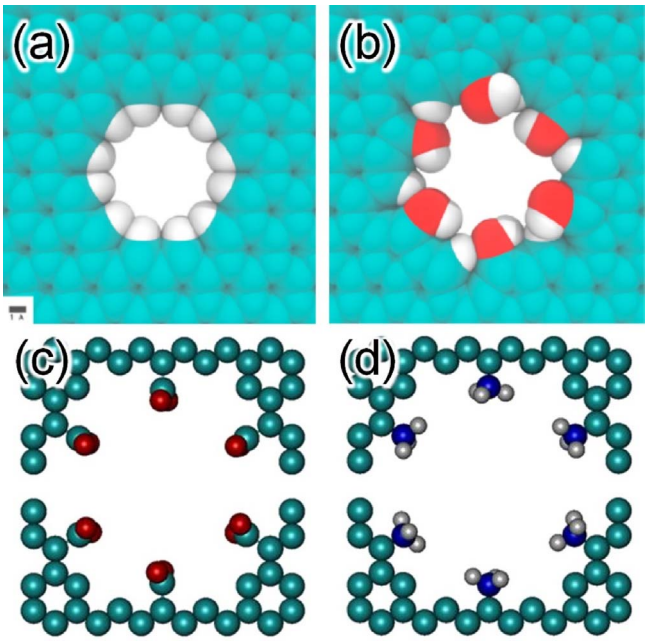


**Fig. 5.** Simulated functionalized graphene pores with (a) $H^+$, (b) $OH^-$, (c) $COO^-$, and (d) $NH^{3+}$. Reprinted with permission from Ref. [80,83]. Copyright 2012 American Chemical Society and Copyright 2013 American Chemical Society, respectively.

under an external electric field. The application of an electric field facilitated the permeation of the $Na^+$ ions through the fluoride (F)-pores and that of $Cl^-$ ions through the hydrogen (H)-pores. The F and H pores were formed by passivating the carbon atoms at the edge of the pores with F and H atoms, respectively.

### 3.1.2. Nanopore generation

Based on the results of these simulation studies on nanoporous graphene membranes, there have been extensive research efforts to produce nanometer-sized pores in graphene in order to be able to use it as a WD membrane. Nanopores can be introduced in graphene by exposing it to an electron beam or by chemical etching, helium ion beam drilling, and other similar methods. A few procedures for forming well-distributed nanosized pores in graphene are shown in Fig. 6. Porous single-layered graphene membranes can be used for desalination when the pore size is controlled to the sub-nanometer scale. At higher densities, sub-nanometer pores can be formed over large graphene surfaces. Given this fact, graphene is irradiated with focused electron beams at voltages higher than the carbon knockout potential, which is ~80 kV, in order to create pores smaller than 3.5 nm. Russo et al. [87] irradiated argon ions over defective graphene to form well-distributed pores of the desired size. Bai et al. [88] extended their work [87] and formed nanopores using ion beam irradiation, while controlling the geometry of the pores by changing the incident angle of the irradiating beam. Oxidative processes have also been used to form pores in graphene; in these processes, graphene is treated with high-temperature atmospheric oxygen, ozone, or hydrogen plasma to create pores. However, these oxidation processes result in pores with different sizes, as the grain boundaries of graphene are more reactive compared to its basal plane [89]. Kim et al. [90] developed a potassium hydroxide activation process for the controlled formation of pores in graphene; using this method, they could form pores with an average size of 3 nm in multilayered graphene. Celebi et al. [91] fabricated atomically thin perforated double-layered graphene with a few million pores having diameters greater than 10 nm; the pores showed high water permeability when the membrane was wetted from both sides.

O'Hern et al. [89] fabricated single-layered graphene by CVD and then introduced defects in the graphene via ion bombardment. Pores with a size of 0.4 nm were then formed using oxidative etching. The etched graphene allowed for selective cation transport, while a longer oxidation time resulted in pores that allowed salt permeation but prevented that of large organic molecules. Recently, Surwade et al. [92] used oxygen plasma etching to create nanopores with a size of 0.5–1 nm in a graphene monolayer, which exhibited a salt rejection rate of 100% and a water flux of $10^6$ g $m^{-2}$ $s^{-1}$ during pressure-driven measurements. The oxygen plasma treatment created defects in the graphene layer within 0.5 s. When the defect concentration was high, with the ratio of the intensity of the Raman D-peak to that of the G-peak ($I_D/I_G$) being approximately 1, the pores were of ~0.5–1 nm in size and the pore number density was 1 pore/100 $nm^2$. However, the measurements were performed over a small area of the graphene sample measuring only 5 μm in diameter. The pores smaller than 2.3 nm were hydrogenated pores, while those smaller than 1.6 nm were hydroxylated pores, which stopped salt and allowed water to permeate.

As discussed above, the narrow pores of graphene are hydrophobic and restrict water permeation. Hence, the pore chemistry plays an important role in water permeation. For example, if the pores are hydrogenated (or hydrophobic), water permeation is restricted whereas the salt rejection performance is enhanced. In contrast, if the pores are hydroxylated (or hydrophilic), water permeation is enhanced whereas the salt rejection performance is limited or altered, depending on the pore size.

The most energy-intensive step in the WD process is the removal of small ionic species, particularly $Na^+$, $K^+$, and $Cl^-$ ions, from water. This is known as ion selectivity and depends on the pore size as well as the charges and functional groups present at the edges of the nanopores. For example, it has been shown that ion-bombarded graphene layers after etching exhibit greater selectivity with respect to positively charged potassium ions instead of chloride ions. This is because of the electrostatic interactions with the negatively charged functional groups present at the edges of the pores. With an increase in the extent of etching, the size of the pores increases, owing to which the ion sieving effect is weakened; however, steric hindrances prevented the passage of dye molecules in this case [89]. Thus, as confirmed by simulation studies, pore functionalization determines whether cations and anions can permeate through the graphene membrane or not. Surwade et al. [92] showed that the ease with which various ions can permeate through pores can be arranged as follows: $Li^+ > Na^+ > K^+$. In order to highlight the effect of ion selectivity, the results of additional reports are listed in Table 2, along with the corresponding salt rejection and water permeation performances.

### 3.2. Stacked GO membranes

GO nanosheets assembled in the form of laminar or stacked structures via filtration contain selective 2D nanochannels and OCGs in a high number density. GO membranes can be mass produced at low costs by means of vacuum filtration, chemical oxidation, or ultrasonic exfoliation. The stacking of GO sheets results in freestanding materials with strong interlayer hydrogen bonds and significantly enhanced mechanical strength. The coexistence of $sp^2$ rings with different functional groups allows for ion sieving; however, GO sheets exhibit a salt rejection rate of only 50%. Nevertheless, GO membranes are effective for rejecting large organic molecules (> 85%) via nanofiltration. Their poor salt rejection performance is owing to the fact that the channels for permeation in the GO sheets swell readily in water because of electrostatic repulsion [93]. Recently Cohen-Tanugi et al. [94] studied multilayered graphene membranes and found that fully aligned pores and very low interlayer distances aid water permeation and salt rejection. A schematic of a GO membrane that also depicts its various physical parameters such as its pore size ($R$), interlayer spacing ($H$), and pore offset ($O$) is presented in Fig. 7. An overview of such GO membranes with similar physical parameters and morphologies for use in WD is given in Table 2. Hegab et al. reported that GO-based membranes can be produced using three techniques [95]: i) fabrication

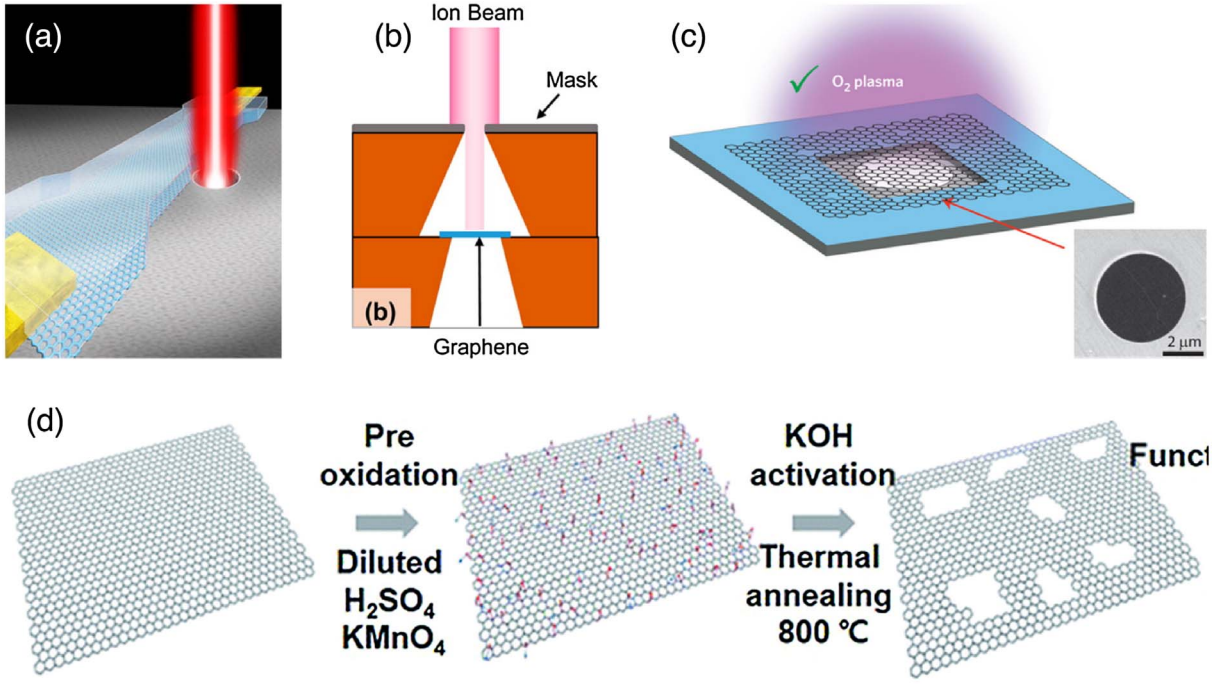


**Fig. 6.** Pore generation methods. (a) Electron beam irradiation. (b) Ion beam irradiation. (c) Oxidative etching. (d) Potassium hydroxide activation. Reprinted with permission from Ref. [152,88]. Copyright 2013 American Chemical Society and Copyright 2016 American Chemical Society. Reprinted by permission from Macmillan Publishers Ltd: Nature Nanotechnology [92], copyright 2015. Reproduced from Ref. [90] with permission of The Royal Society of Chemistry.

of freestanding GO, ii) application of GO on the surface of a membrane, and iii) mixing GO with a polymer to create a mixed-matrix membrane.

### 3.2.1. *Freestanding GO membranes*

Sun et al. [96] prepared freestanding membranes using GO flakes modified by Hummers' method using the drop-casting method. The membranes were dried and used as filters with a diameter of 5 mm. Sodium salts permeated quickly ($NaOH > NaHSO_4 > NaCl > NaHCO_3$) through the membranes whereas heavy metal ions penetrated slowly because of the tight coordination between the functional groups of the GO sheets. When the GO membranes were wetted and the interlayer distance was increased, water filled the nanocapillaries and permeated the membranes. Because of the iontophoretic injection process, anions could permeate through the capillaries; however, cations could not, owing to the strong repulsive forces between the cations and the functional groups. In another study, Sun et al. [97] observed the presence of $sp^2$ clusters and found that the cation–π interactions improved the ion rejection performance of the GO membranes.

The ability of GO membranes to reject salts is lost as the membrane thickness is increased. The interlayer spacing between the GO sheets is of critical importance with respect to ion sieving; a higher membrane thickness increases the interlayer spacing. The required interlayer spacing for GO membranes for salt removal is less than 0.3 nm. In the case of a GO spacing of 0.7 nm [98], the radii of hydrated $Na^+$ and $K^+$ ions are smaller than the spacing; this allows the ions to flow through the membrane along with water molecules. When immersed in ionic solutions, the GO sheets get hydrated and the spacing increases to 0.9 nm; this weakens the sieving effect. When the interlayer spacing is reduced to less than 0.6 nm, the amount of OCGs decreases. As a result, the nanocapillary action of the sheets is eliminated and water can no longer permeate through them [99]. Thus, reducing the interlayer

**Table 2**
Graphene and GO membranes for WD.

| Membrane | Surface property | Selectivity transport of Ions | Salt removal | Water permeance | Ref |
|---|---|---|---|---|---|
| Graphene | – | $K^+$ (5 min etching) | – | – | [89] |
| Graphene | – | $K^+$ (20 nm pore diameter) | – | – | [153] |
| Graphene | Hydrophobic (115°) | | 84% (KCl)- | – | [154] |
| Graphene | – | $Li^+ > Na^+ > K^+$ | 100% (NaCl) | 106 [g $m^{-2}$ $s^{-1}$ $atm^{-1}$] | [92] |
| Graphene | – | – | 70% ($MgSO_4$) | 1.41 ± 0.23 [L $m^{-2}$ $h^{-1}$ $bar^{-1}$] | [155] |
| Multilayer Graphene | – | – | 20% (NaCl) | 37 [L $m^{-2}$ $h^{-1}$ $bar^{-1}$] | [90] |
| GO | Hydrophilic | Heavy metal salts $Na^+ > Mn^{2+} > Cd^{2+} > Cu^{2+}$ | – | – | [96] |
| GO | – | – | 99.7% | 48.4 [kg $m^{-2}$ $h^{-1}$ $atm^{-1}$] | [156] |
| GO + PTFE + HFP | Hydrophobic (90.6°) | – | 100% | 97 [kg $m^{-2}$ $h^{-1}$ $atm^{-1}$] | [101] |
| GO + PDI | Hydrophilic (28.9°) | | 99.9% (seawater) | – | [102] |
| GO + TMPyP | – | – | 87.7% ($Na_2SO_4$) | – | [93] |
| GO + PDA | – | $KCl > MgCl_2 > CaCl_2 > NaCl$ | – | 7.3 [L $m^{-2}$ $h^{-1}$ $bar^{-1}$] | [103] |
| GO + PSf | Hydrophilic (53°) | – | 72% ($Na_2SO_4$) | 5 [L $m^{-2}$ $h^{-1}$ $bar^{-1}$] | [104] |
| GO + PSf | Hydrophilic (56°) | – | 97% (NaCl) | 1.97 [L $m^{-2}$ $h^{-1}$ $bar^{-1}$] | [105] |
| GO + OCMC + PSf | Hydrophilic (49.8°) | | 62% (NaCl) and 92% ($Na_2SO_4$) | 27 [L $m^{-2}$ $h^{-1}$@1.5 MPa] | [106] |
| GO + PEI + PAN | Hydrophilic (58°) | $Na_2SO_4 > MgSO_4 > MgCl_2 > NaCl$ | 80.9% ($MgCl_2$) | 65.6 [L $m^{-2}$ $h^{-1}$@0.40 MPa] | [107] |

HFP – hexafluoropropylene, TMPyP – tetrakis(1-methyl-pyridinium-4-yl)porphyrin.

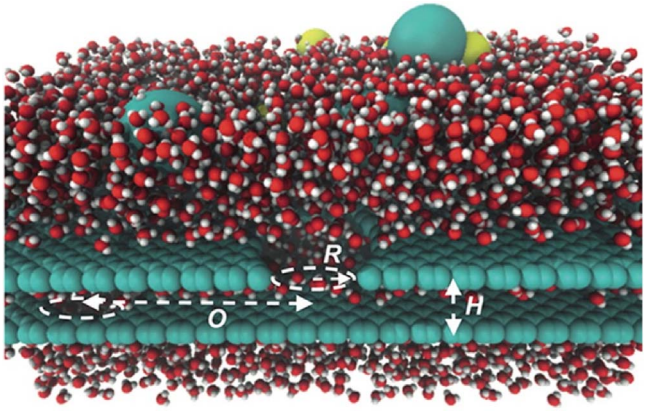


**Fig. 7.** Bilayer graphene showing pore size (R), interlayer spacing (H), and pore offset (O). Reprinted with permission from Ref. [94]. Copyright 2016 American Chemical Society.

spacing for the removal of NaCl based on the concept of size exclusion and water transport through nanocapillaries remains a significant challenge with respect to the commercialization of GO membranes.

*3.2.2. GO-modified polymer membranes*

It is expected that applying GO on the surfaces of polymer membranes will improve the mechanical strength and separation performance of the membranes. To produce such membranes, a thin few-nanometers-thick layer of GO is deposited onto a thick support (> 10 μm) by vacuum filtration, drop casting, or layer-by-layer coating. These GO layers are thinner than those that make up freestanding GO membranes. Hu et al. [100] coated GO sheets onto polysulfone (PSf) supports, wherein the GO sheets were held together because of a cross-linking process. The water flux was observed to be 8–27 $L\,m^{-2}\,h^{-1}\,bar^{-1}$. Bhadra et al. [101] immobilized GO on the surface of a polytetrafluorethylene (PTFE) membrane for desalination via direct-contact membrane distillation. The use of GO changed the contact angle of PTFE from 110° to 90.6°. The membrane exhibited good salt rejection performance because of the screening effect of the nanopores on the GO surface, in addition to water permeation. Feng et al. [102] used an 18-μm-thick GO membrane prepared on 1,4-phenylene diisocyanate (PDI) for desalination. The membrane showed a high water flux and a desalination rate of more than 99.9% in the case of 3.5 wt% seawater during pervaporation. The WCA (28.9°) of the membrane indicated that it was hydrophilic (Table 2).

*3.2.3. Mixed-matrix membranes*

In order to increase the water permeation and salt rejection performances, new methods for adding GO to mixed polymer solutions have been proposed. These GO-containing solutions are then cast into membranes, which are called mixed-matrix membranes [103]. It is expected that the OCGs of GO will form strong hydrogen-bond networks with the water molecules, owing to which the GO will exhibit desirable hydrophilic properties, which will help restrict fouling. Ganesh et al. [104] prepared a membrane by blending GO with hydrophobic PSf; the membrane showed a $Na_2SO_4$ rejection rate of 72%, with the water permeance being approximately 5 $L\,m^{-2}\,h^{-1}\,bar^{-1}$. Membranes of reduced GO (rGO) with polydopamine (PDA) matrices were fabricated by vacuum filtration. The salt rejection performance of the membranes was 15 times better while their water flux was 12 times higher than those of pristine PDA and pristine GO [103]. Ali et al. [105] prepared thin films of a composite using GO and PSf; the thin films showed an NaCl removal rate of 97% and a water flux of 1.97 $L\,m^{-2}\,h^{-1}\,bar^{-1}$. **(R1-2)** Wang et al. [106] fabricated nanofiltration membranes by coating *O*-(carboxymethyl)-chitosan (OCMC) on PSf membranes. The membranes were soaked in a dispersion of GO nanosheets with epichlorohydrin (ECH); this not only resulted in the cross-linking of ECH and OCMC but also the bonding of the epoxy group of GO with the amino group. The membranes prepared by soaking in 100 mg/L of the GO nanosheet dispersion exhibited enhanced hydrophilicity, showing monovalent (NaCl) and divalent ($Na_2SO_4$) salt rejection rates of 62 and 93%, respectively. More recently, Wang et al. [107] formed a GO layer on a hydrolyzed polyacrylonitrile (PAN) substrate with polyethyleneimine (PEI) in a layer-by-layer manner using an external electric field. The optimized membrane composed of 2 PEI/GO bilayers showed hydrophilicity, high water permeance, and a salt rejection rate of 80.9%. Such mixed-matrix membranes can be used for WD through reverse osmosis, membrane distillation, and pervaporation.

GO membranes are hydrophilic owing to the presence of OCGs. For this reason, even when a small amount of GO is mixed with polymeric materials such as PDI and PSf, the resulting mixed membranes show hydrophilicity and enhanced water permeation. Water molecules can pass through the GO channels while the hydrophilic functional groups in the GO facilitate the adsorption of the water molecules onto the membrane surface. Both effects aid water transport.

## 4. Purification of water

### 4.1. Adsorption properties of GO and rGO

GO, the oxidized phase of graphene, contains OCGs such as −COOH, −C═O, and −OH on its surface. The sites of these functional groups can anchor metal ions to the GO surface through electrostatic interactions and coordination [2,108]. Because of the high affinity of oxygen atoms for metal ions, these OCGs increase the adsorption ability of GO. Moreover, the hydrophilicity of GO induced by the OCGs improves its water dispersibility [109]. Thus, GO can be used in aquatic environments such as wastewater and water bodies containing microorganisms for filtering tetracyclines [110], methylene blue (MB) [20], aromatic organic compounds [111], and heavy metals [112] (cf. Tables 3 and 4). However, it should be noted that uncontaminated pure graphene is not appropriate for use as an adsorptive material even though it has recently been shown to be hydrophilic. This is because the intrinsic hydrophilicity of graphene is not related to the presence of the OCGs, as described in Section 2.1. In the case of rGO, most of the OCGs are removed during the reduction process. Hence, the adsorption capacity of rGO is much lower than that of GO. The various advantages of rGO, including its large surface area and high stability, make it suitable for combining with other materials for the removal of heavy metal ions and toxic elements. The hydrophilic nature of GO with a large negative charge on its surface allows for the effective removal of cationic impurities such as heavy metals and toxic organic molecules. In addition, the OCGs on the GO surface result in a large negative zeta potential, which helps inactivate bacteria and restricts biofouling originating from microbial adsorption. For example, a synthesized magnetite-rGO composite was used to separate more than 99.9% of the arsenic present in water in a concentration of 1 ppb [113]. Sreeprasad et al. demonstrated that rGO-$MnO_2$ and rGO-Ag are effective adsorbents, exhibiting uptake rates greater than 10 $L\,g^{-1}$ in the case of mercury(II), which was used as a model pollutant [114]. $TiO_2$ is another material used for enhancing the photocatalytic activities of graphene and GO [115–118] (cf. Table 3). In addition, the adsorption capacity of a material can be enhanced by changing parameters such as the pH of the environment [119], the porosity of its structure [120], and the contact time [19]. The surface charge and electrostatic interactions are directly influenced by the changes in the pH. As the porosity of the adsorbent increases, the likelihood of pollutants coming in contact with it also increases. To make graphene porous, other porous materials can be combined with it [121]. In addition, graphene materials with three-dimensional (3D) architectures can be fabricated [120,122,123]. The various forms and structures of graphene are reviewed in the following section.

**Table 3**
Removal efficiency and adsorption capacity of graphene composites.

| Composite | Typical parameters of experiments | Removal efficiency [%] | Adsorption capacity [mg $g^{-1}$] | Ref |
|---|---|---|---|---|
| GO | Aniline | | 115.1 | [111] |
| | Nitrobenzene | | 68.7 | |
| | Chlorobenzene | | 67.2 | |
| $TiO_2$/GO | Rhodamine B, A07 | 50 | | [116] |
| $TiO_2$/GO | Methyl orange | 100 | | [117] |
| | Rhodamine B | | | |
| G-sand composite | Rhodamine 6G | | 75.4 | [132] |
| GO/layered double hydroxides | Methylene blue | | 125 | [133] |
| CNT/rGO | Methyl orange | 97.3 | | [136] |
| | Titan yellow | > 99 | | |
| | Chlorazol black | > 99 | | |
| | Chlorazol fast pink | > 99 | | |
| | Direct red 80 | > 99 | | |
| $TiO_2$/GO | Methyl orange | 70 | | [138] |
| $Fe_2O_3$/GO | Rhodamine B | 40 | | [139] |
| $Fe_3O_4$/rGO | Rhodamine B | 91 | | [141] |
| | Malachite green | 94 | | |
| GO/chitosan | Methylene blue | | 390 | [142] |
| | Eosin Y | | 326 | |
| Graphene/carbon/MWCNT | Methylene blue | | 190.9 | [147] |
| | Rhodamine B | | 145.9 | |
| PEI/rGO/Ag | Methylene blue | 100 | 35.25 | [157] |
| | Rhodamine B | | 13.5 | |
| MgSi@rGO | Acid brilliant blue | 98.2 | | [158] |
| | Chrome blue-black R | 95.2 | | |
| | Methyl orange | 73.4 | | |
| GO/$TiO_2$/PVDF | Bovine serum albumin | 92.5 | | [159] |

**Table 4**
Metal ion adsorption capacities of graphene composites for various parameters.

| Composite | Typical parameters of experiments | Adsorption capacity [mg $g^{-1}$] | Ref |
|---|---|---|---|
| GO | Tetracycline | 313 | [110] |
| GO | $Hg^{2+}$ | 35 | [112] |
| $Fe_3O_4$/rGO | $As^{3+}$ | 13.1 | [113] |
| | $As^{5+}$ | 5.83 | |
| HMO@GO | $Pb^{2+}$ | 553.6 | [130] |
| GO/layered double hydroxides | $Cd^{2+}$ | 95.67 | [133] |
| GO/chitosan | $Cu^{2+}$ | 63 | [142] |
| | $Pb^{2+}$ | 95 | |
| 2,6-diamino pyridine/rGO | $Cr^{6+}$ | 393.68 | [145] |
| Iron nanoparticles/graphene | $Cr^{6+}$ | 162 | [146] |
| | | 148 | |
| Graphene/acid treated MWCNT | $Pb^{2+}$ | 104.9 | [147] |
| | $Hg^{2+}$ | 93.3 | |
| | $Ag^{2+}$ | 64 | |
| | $Cu^{2+}$ | 33.8 | |
| $SiO_2$/graphene | $Pb^{2+}$ | 113.6 | [148] |
| Magnetic chitosan/graphene | $Pb^{2+}$ | 76.94 | [149] |
| $MnO_2$/graphene nanosheet | $Ni^{2+}$ | 46.6 | [150] |
| GO | $Cu^{2+}$ | 46.6 | [151] |

### 4.2. Synthetized structure

Graphene is mostly produced by direct growth on metal substrates [124], micromechanical exfoliation [125], exfoliation in a solvent [126], and through substrate-free gas-phase synthesis [127]. Recently, GO was fabricated by the oxidation of graphite and reduced to rGO by thermal or electrochemical treatments. The main route for preparing GO sheets from graphite is the modified Hummers' method [128,129]. In this method, graphite is oxidized using potassium permanganate ($KMnO_4$) and sulfuric acid ($H_2SO_4$).

In most cases, the synthesized GO flakes remain dispersed in the aqueous waste solution after use [113,130,131]. However, the removal of the residual GO after the completion of the adsorption process requires further filtration. For example, it is difficult to remove GO dispersed in a solution because of the small size of the GO flakes. For this reason, GO is immobilized in various forms and structures. The immobilization of GO is also beneficial with respect to the cyclic adsorption–desorption process [19,132]. The repeatable use of an adsorbent is essential for it to have high applicability.

Graphene flakes are assembled in 3D network-like structures through entrapment between nanofiber layers [19]. The structured graphene in the purification membrane is effective for both the adsorption and the desorption of the pollutant molecules. Similarly, thin robust membranes assembled using 2D graphene sheets are advantageous because of their low cost and high performance [18,121]. Fabrication processes using vacuum filtration or dip-coating approaches are simple and scalable for mass production, in contrast to most of the processes used for producing nanofiltration membranes, which have several drawbacks, including complex fabrication processes and high cost. Thus, the proposed method is promising for use in numerous applications, including wastewater treatment and purification.

In another method, rGO was bound to river sand, which is cheap and abundant. The rGO-coated sand was used as a low-cost contaminant-removing material [114]. Graphene-sand composites (GSCs) can also be synthesized using asphalt as the carbon precursor [132]. These materials exhibit higher strength, reusability, and adsorption capacity.

As a representative 3D macroscopic structure, a GO foam was developed by Henriques et al. [112] (Fig. 8). The 3D macrostructure was fabricated by the simple self-assembly of GO sheets. The surface chemistry was modified through functionalization with nitrogen and sulfuric groups containing oxygen atoms; the removal efficiency of the

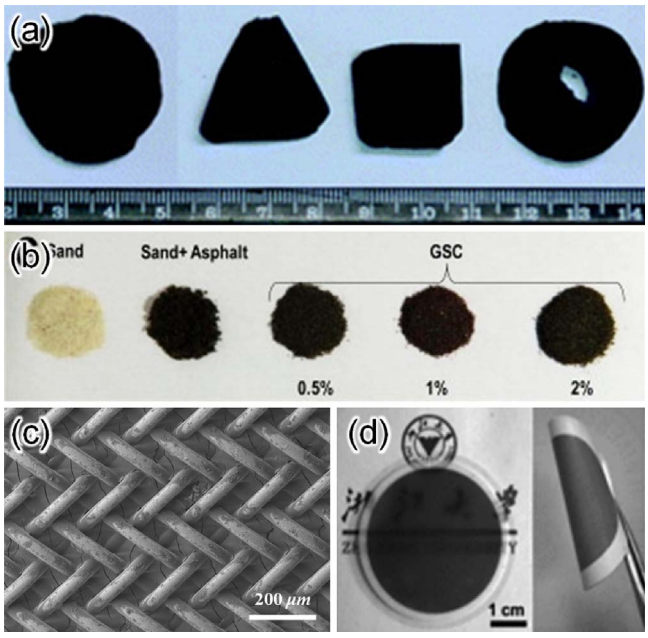


**Fig. 8.** The immobilized form of GO on (a) sponge, (b) sand, and (c)(d) membrane filter. Reproduced from Ref. [123] with permission of The Royal Society of Chemistry. Reprinted from permission from Ref. [132]. Copyright 2010 with permission from Elsevier. Reprinted with permission from Ref. [18]. Copyright 2014 American Chemical Society. Reprinted from permission from Ref. [135].

GO foam with respect to mercury(II) was evaluated and was found to be 96% under certain conditions.

Self-assembled GO aerosols and hydrogels have been prepared through facile one-step methods [133]. These 3D networks of graphene exhibited hydrophilicity, high structural stability, and high removal rates for MB and cadmium(II) as pollutants in aqueous environments. Their structure, which is a convenient one to fabricate, results in a high adsorption capability. Mi et al. also prepared porous GO aerogels and evaluated their adsorption performance with respect to copper(II) ions [134]. They successfully synthesized GO aerogels with oriented pore structures by a unidirectional freeze-drying method. The interconnected pore structure of the GO aerogels enhanced the adsorption rate by promoting the diffusion of metal ions to the adsorption sites.

### 4.3. Target contaminants

#### 4.3.1. Removal of organic compounds

Graphene has been used for water purification membranes because of its unique microstructure and physicochemical properties. Sreeprasad et al. [132] fabricated graphene-based materials from cheaper precursors, such as asphalt, and immobilized these materials on sand particles. The resulting GSC was used for the removal of a dye (rhodamine 6G). The adsorption capacity of the GSC was calculated to be 75.4 mg $g^{-1}$ (Table 3). Han et al. [135] fabricated purification membranes using chemically converted ultrathin graphene (thickness of 22–53 nm) with 2D nanochannels by a simple filtration method. The ultrathin graphene nanofiltration membranes showed a high pure water flux (21.8 L $m^{-2}$ $h^{-1}$ $bar^{-1}$) as well as a high retention rate for organic dyes (MB and Direct Red 81) and a moderate one for salt. A GO-Nylon 6 nanofiber membrane formed on a stainless steel mesh was also used for water purification [19,20]. It could successfully remove the model pollutant, MB; this was accomplished through the adsorption of the MB molecules onto the GO surface. Chen et al. [136] developed a rGO hybrid nanofiltration membrane with CNTs for the purification of drinking water; the membrane was fabricated by a vacuum-assisted filtration process. They measured the permeability and retention properties of the membrane using dyes (Direct Red 80, chlorazol fast pink, chlorazol black, titan yellow, and methyl orange (MO)) with different molecular weights. The membrane had a high retention efficiency (97.3%) for MO and showed a high permeability (20–30 L $m^{-2}$ $h^{-1}$ $bar^{-1}$) (Table 3).

GO-$TiO_2$ composites have also been fabricated through various methods. GO has been used as a cross-linker and electron acceptor for $TiO_2$. $TiO_2$ is used as a membrane material because of its good photocatalytic characteristics. For this reason, a GO-$TiO_2$ composite was used to remove organic dyes from aqueous solutions, and its photocatalytic properties were characterized under UV and visible light.

Xu et al. [137] successfully synthesized GO-$TiO_2$ composite films using vacuum filtration. The GO-$TiO_2$ membranes could successfully remove dye molecules (MO and rhodamine B, 10 ppm); it also arrested additional amounts of both types of dye molecules. They also demonstrated that the GO-$TiO_2$ membranes could be used for other purposes as well, such as filtration. Gao et al. [116] fabricated a GO-$TiO_2$ microspheres-based hierarchical membrane on a cellulose acetate membrane. The performance of the GO-$TiO_2$ membrane was evaluated via (1) the degradation of rhodamine B and A07; (2) flux measurements; (3) measurements of its mechanical properties; and (4) measurements of its antifouling performance. It was found that GO enhanced the specific surface area of $TiO_2$, in addition to improving electron transfer, which resulted in enhancements in the photocatalytic performance. Athanasekou et al. [118] developed ceramic membranes by forming a GO-$TiO_2$ composite on a ceramic ultrafiltration membrane and a nanofiltration membrane via dip-coating and tested their photocatalytic degradation performances using the synthetic dyes MO and MB. GO-$TiO_2$ showed high performance, using 20 times less energy than is the case during standard nanofiltration processes. Filice et al. [138] prepared hybrid nanocomposite Nafion membranes containing GO and $TiO_2$ by the solvent-casting method for water purification. The photocatalytic activity of the hybrid Nafion membranes was assessed based on the removal of a dye (MO) under UV/visible light illumination. The membranes showed very good performances (cf. Table 3).

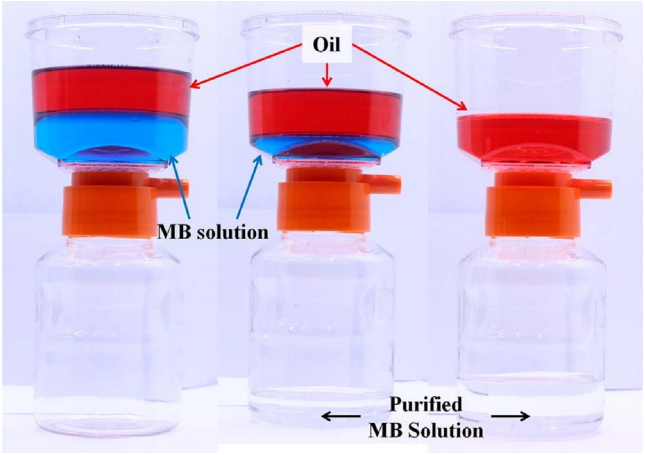


**Fig. 9.** Detailed oil-MB separation capability and purification of MB by composite membrane. Reprinted with permission from Ref. [18]. Copyright 2014 American Chemical Society.

Yoon et al. [18] demonstrated the purification of water and the separation of oil from water using a graphene plug and a hydrophilic/oleophobic composite membrane (Fig. 9). MB was used as the model dye for wastewater. The proposed technique for fabricating the membranes for the separation of oil and water as well as water purification was a simple one and can be scaled for mass production.

Because of its physicochemical properties and potential for use in water splitting and catalysis, $Fe_2O_3$ has been studied extensively. Guo et al. [139] synthesized a GO-$Fe_2O_3$ hybrid material for the degradation of organic contaminants and evaluated its performance with respect to the degradation of rhodamine B and 4-nitrophenol in an aqueous solution under visible-light irradiation (> 420 nm) (cf. Table 3).

Pawar et al. [140] reported a single-crystal hematite ($Fe_2O_3$)/rGO/multiwalled carbon nanotubes (MWCNTs) composite, which was synthesized by a hydrothermal method. The composite was evaluated based on the degradation of rhodamine B under visible-light irradiation. Various characterization techniques suggested that the $Fe_2O_3$/rGO/MWCNTs composite had a significantly higher specific surface area and optical absorbance compared to those of $Fe_2O_3$, $Fe_2O_3$/MWCNTs, and $Fe_2O_3$/rGO, as well as a reduced charge-carrier recombination rate.

Sun et al. [141] developed a magnetite ($Fe_3O_4$)/rGO (MrGO) nanocomposite using a simple one-step method for use in the removal of dye pollutants. The MrGO composite showed good adsorption efficiency (> 91% for rhodamine B, > 94% for malachite green) (Table 3).

Chitosan (CS) has been studied widely because of its potential for use as an absorbent for metal ions and anionic dyes. However, it exhibits mechanical instability. GO-CS hydrogels, formed via the self-assembly of GO sheets and CS chains, were used as absorbents to remove dyes (MB and eosin Y) [142]. The absorption capabilities of the hydrogels were determined for different relative contents of GO and CS. In the case where the GO content was higher, the adsorption capacity for MB was higher as well. Therefore, the GO and CS contents should be controlled based on the dye pollutant to be removed. Fig. 10 and Table 3 show the removal of pollutants from water by filtration using the GO-CS hydrogels and the absorbance of the decolorized water sample after filtration.

Meidanchi et al. [143] synthesized a superparamagnetic $ZnFe_2O_4$/

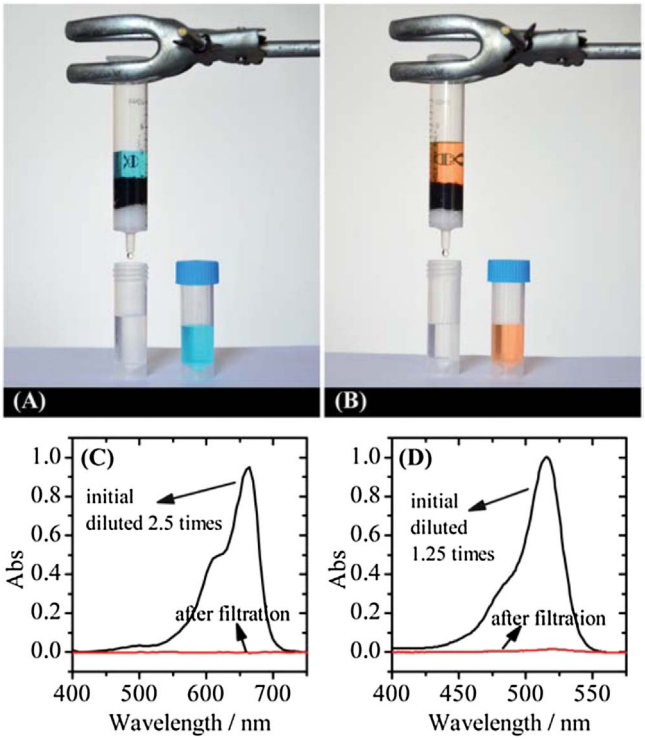


**Fig. 10.** (a, b) Snapshot showing removal of dyes from water. Absorption spectra of the (c) MB and (d) Eosin Y. Reproduced from Ref. [142] with permission of The Royal Society of Chemistry.

rGO composite by a hydrothermal reaction. They reported that the magnetic separation times for MO and rhodamine B changed with the $ZnFe_2O_4$ and rGO contents in the composite. Compared to pure $ZnFe_2O_4$, the $ZnFe_2O_4$/rGO composite needed less time to separate the two dyes.

Fang et al. [133] fabricated layered double hydroxides (LDH)/GO aerogels by a self-assembly approach. LDH was used as a cross-linker between the molecules. The adsorption capacity of the LDH/GO aerogel for MB (96–125 mg $g^{-1}$) was 94% higher than that of the LDH powder alone. Liang et al. [144] prepared a MgSi@rGO/polyacrylonitrile (PAN) composite membrane via a vacuum filtration method. The fabricated MgSi@rGO/PAN composite membrane was evaluated by using it to remove dyes (acid brilliant blue, chrome blue-black R, and MO) with different molecular weights from water. In the case of acid brilliant blue, the rejection rate was 98.2%.

In addition, GO has been used as an effective absorbent for pharmaceutical products because of its hydrophilicity, suitable structure, and high surface area. For example, tetracycline is a widely used antibiotic and consists of phenol, alcohol, ketone, and amino groups. Gao et al. [110] synthesized a GO stock solution (pH 3.6) and mixed it with a tetracycline solution. The adsorption capacity of GO was very high under low pH conditions; it was also observed that the temperature did not have a significant effect.

#### 4.3.2. Metal ion removal

Wastewater from many industries contains different types of heavy metal ions such as those of arsenic, mercury, cadmium, and chromium. The removal of these harmful metal ions from wastewater remains a significant challenge. Graphene is an excellent absorbent and can be used for removing various pollutants. Chromium primarily exists in two oxidized states, namely, as chromium(III) and chromium(VI). Dinda et al. [145] synthesized a UV-active diamino pyridine-RGO composite for treating water contaminated with chromium(VI) via a simple $S_N2$ substitution technique (cf. Table 4).

Jabeen et al. [146] synthesized iron-decorated graphene using a sodium borohydride reduction reaction. The hybrid material had a high surface area (170 $m^2$ $g^{-1}$) and small particle size (10 nm) and was used as an absorbent to remove chromium(VI). It showed a maximum adsorption capacity of 162 mg $g^{-1}$ (Table 4).

CNT/graphene hybrid aerogels fabricated via supercritical $CO_2$ drying have shown promising results in water purification, including in the removal of heavy metal ions [147]. The aerogels had binding capacities of 104.9, 93.3, 64, and 33.8 mg $g^{-1}$ with respect to lead(II), mercury(II), silver(I), and copper(II), respectively (Table 4). As mentioned in the previous section, Chen et al. [142] fabricated a GO-CS hydrogel for use as an absorbent. It was also used as an absorbent for heavy metal ions. The maximum adsorption capacities of the hydrogel for copper(II) and lead(II) were 63 and 95 mg $g^{-1}$, respectively, with the capacities being determined by the component ratio.

Although iron oxides ($Fe_xO_x$) are highly efficient materials for removing arsenic, they are difficult to use because of their instability. Arsenic is a representative pollutant found in wastewater. Chandra et al. [113] synthesized a magnetite/rGO (M-rGO) hybrid powder via a chemical reaction for removing arsenic. The obtained adsorption data for different arsenic concentrations at $T$ = 20 °C and pH = 7 could be fitted with the Freundlich and Langmuir isotherm models. They also found that the adsorption capacity of the M-rGO composite was the highest for arsenic(III) and arsenic(V). In addition, they investigated the effects of the temperature and pH on arsenic adsorption. The results showed that the composites had a high adsorption capacity. Henriques et al. [112] prepared a GO foam in which nitrogen functional groups or nitrogen (3DGON) and sulfur functional groups (3DGOSN) were combined and used it for removing mercury(II). They evaluated the performance of the GO foam with respect to the removal of mercury(II) under various conditions by changing the pH, sorbent dose, and time and by having other metal ions present as well. A small amount of 3DGON (10 mg $L^{-1}$) could remove 95% of the mercury(II) present within 24 h. Sreeprasad et al. [132] synthesized rGO-$MnO_2$ and rGO-Ag composites and found that they showed better mercury(II) removal capacities as compared to those of the parent materials. They also developed a method for anchoring the rGO-composites onto particles of river sand.

Wan et al. [130] fabricated nanosized hydrated manganese oxide on GO (HMO@GO) to overcome the limitations of GO. Even in the presence of several competing materials, such as calcium(II), magnesium(II), and humic acid (HA), the HMO@GO composite removed lead (II) selectively. Furthermore, it could be reused after treatment with 0.3 M HCl. Hao et al. [148] synthesized a $SiO_2$/graphene composite via a simple method for use as an absorbent for lead(II). The composite had a high surface area, high binding capability, and significant adsorption capability with respect to lead(II). The maximum adsorption capacity of the $SiO_2$/graphene composite was 113.6 mg $g^{-1}$ (Table 4). Fan et al. [149] demonstrated that a magnetic chitosan/graphene (MCGO) composite is an excellent absorbent for lead(II) in water and can be fabricated via a simple and quick process. The MCGO composite showed a high adsorption capacity (76.84 mg $g^{-1}$) at lower pH values, with its desorption efficiency being 90.3% (Table 4).

$MnO_2$ has drawn great interest because of its physical and chemical properties. However, the complexity of its synthesis process and the fact that it is difficult to control its morphology limit its applicability. Ren et al. [150] fabricated a δ-$MnO_2$/graphene nanosheet ($MnO_2$/GNS) composite via a microwave-assisted method for use as an adsorbent for nickel(II) in wastewater. The maximum adsorption capacity of the $MnO_2$/GNS composite was determined to be 46.6 mg $g^{-1}$ (Table 4). In addition, after five adsorption–desorption cycles in 0.1 M HCl, the $MnO_2$/GNS composite showed a recovery rate as high as 91%.

Finally, GO is also used as an absorbent for removing copper from contaminated water. Yang et al. [151] found that GO is folded and aggregated by copper(II) in aqueous solutions. The folding and aggregation of GO is caused by interactions between copper(II) and the oxygen atoms on the GO surface; these interactions are the primary

driving force for the adsorption process (cf. Table 4). Further, the adsorbed copper(II) can be desorbed by a simple process.

## 5. Future directions

The intrinsic wettability of pure graphene is not clearly hitherto identified. However, in order to able to effectively exploit this property of graphene in various engineering fields, time-independent hydrocarbon-free methods for fabricating and modifying it need to be developed. We suggest that this should begin with the development of anti-hydrocarbon coatings for graphene that result in the generation of a repulsive force between the graphene and various hydrocarbons. Simultaneously, cost-effective methods for modifying the wettability of graphene in the form of GO and rGO should also be developed to further the use of the existing economically viable graphene-based materials in WD and purification. Graphene-based materials have already shown excellent performances when used in WD and purification. The development of industrially scalable and economically viable processes for fabricating graphene and graphene-based materials will help in overcoming the challenges arising from the incompatible requirements for simultaneously ensuring a high water flux and good salt rejection performance.

## 6. Conclusions

Although studies on the intrinsic wetting characteristics of graphene have recently shown that graphene is essentially hydrophilic, additional studies on the uses of graphene have reported that it shows hydrophobic features because of the presence of inevitable defects and owing to the fact that it is usually employed in forms with a multilayered structure. Accordingly, modification methods for ensuring that it shows superhydrophobicity are being investigated extensively. The extraordinary wetting behavior of graphene, as well as its unique 2D porous structure, make it highly attractive for use in WD and purification. In particular, GO membranes with controlled interlayer spacings and pore sizes could be an affordable option for high-performance WD. The functionalization of the GO membranes and the formation of mixed matrices with the GO surfaces would simultaneously improve the salt rejection capability and water permeation. In addition, owing to the OCGs present on its surface, GO has a high adsorption ability, which is advantageous with respect to water purification applications. Furthering our understanding of the properties of graphene and the development of novel methods for fabricating and modifying it should lead to even greater improvements in the fields of WD and purification.

## Acknowledgements

This research was supported by Korea University Future Research Grant and also by Business for Cooperative R & D between Industry, Academy, and Research Institute funded Korea Small and Medium Business Administration (C0421241). This research was also supported by Global Frontier Program through the Global Frontier Hybrid Interface Materials (GFHIM) of the National Research Foundation of Korea (NRF) funded by the Ministry of Science, ICT & Future Planning (2013M3A6B1078879) and the Technology Development Program to Solve Climate Changes of the National Research Foundation (NRF-2016M1A2A2936760).

## References

[1] A.K. Geim, K.S. Novoselov, Nat. Mater. 6 (2007) 183–191.
[2] Y. Zhu, S. Murali, W. Cai, X. Li, J.W. Suk, J.R. Potts, R.S. Ruoff, Adv. Mater. 22 (2010) 3906–3924.
[3] K.S. Novoselov, A.K. Geim, S.V. Morozov, D. Jiang, Y. Zhang, S.V. Dubonos, I.V. Grigorieva, A.A. Firsov, Science 306 (2004) 666–669.
[4] A.A. Balandin, S. Ghosh, W. Bao, I. Calizo, D. Teweldebrhan, F. Miao, C.N. Lau, Nano Lett. 8 (2008) 902–907.
[5] K.S. Novoselov, V. Fal, L. Colombo, P. Gellert, M. Schwab, K. Kim, Nature 490 (2012) 192–200.
[6] V.Y. Aristov, G. Urbanik, K. Kummer, D.V. Vyalikh, O.V. Molodtsova, A.B. Preobrajenski, A.A. Zakharov, C. Hess, T. Hänke, B. Buchner, Nano Lett. 10 (2010) 992–995.
[7] S. Bae, H. Kim, Y. Lee, X. Xu, J.-S. Park, Y. Zheng, J. Balakrishnan, T. Lei, H.R. Kim, Y.I. Song, Nat. Nanotechnol. 5 (2010) 574–578.
[8] S. Garaj, W. Hubbard, J. Golovchenko, Appl. Phys. Lett. 97 (2010) 183103.
[9] M. Lotya, P.J. King, U. Khan, S. De, J.N. Coleman, ACS Nano 4 (2010) 3155–3162.
[10] E.P. Randviir, D.A. Brownson, C.E. Banks, Mater. Today 17 (2014) 426–432.
[11] L. Liao, Y.-C. Lin, M. Bao, R. Cheng, J. Bai, Y. Liu, Y. Qu, K.L. Wang, Y. Huang, X. Duan, Nature 467 (2010) 305–308.
[12] X.D. Zhuang, Y. Chen, G. Liu, P.P. Li, C.X. Zhu, E.T. Kang, K.G. Noeh, B. Zhang, J.H. Zhu, Y.X. Li, Adv. Mater. 22 (2010) 1731–1735.
[13] J. Wu, M. Agrawal, H.A. Becerril, Z. Bao, Z. Liu, Y. Chen, P. Peumans, ACS Nano 4 (2009) 43–48.
[14] H. Kim, K.-Y. Park, J. Hong, K. Kang, Sci. Rep. 4 (2014) 2045–2322.
[15] Z. Yin, J. Zhu, Q. He, X. Cao, C. Tan, H. Chen, Q. Yan, H. Zhang, Adv. Energy Mater. 4 (2014) 1300574.
[16] M.G. Chung, D.H. Kim, H.M. Lee, T. Kim, J.H. Choi, D. kyun Seo, J.-B. Yoo, S.-H. Hong, T.J. Kang, Y.H. Kim, Sens. Actuators B 166 (2012) 172–176.
[17] D.Y. Kim, S. Sinha-Ray, J.J. Park, J.G. Lee, Y.H. Cha, S.H. Bae, J.H. Ahn, Y.C. Jung, S.M. Kim, A.L. Yarin, Adv. Funct. Mater. 24 (2014) 4986–4995.
[18] H. Yoon, S.-H. Na, J.-Y. Choi, S.S. Latthe, M.T. Swihart, S.S. Al-Deyab, S.S. Yoon, Langmuir 30 (2014) 11761–11769.
[19] S. An, H.S. Jo, K.Y. Song, M.G. Mali, S.S. Al-Deyab, S.S. Yoon, Nanoscale 7 (2015) 19170–19177.
[20] J.-G. Lee, D.-Y. Kim, M.G. Mali, S.S. Al-Deyab, M.T. Swihart, S.S. Yoon, Nanoscale 7 (2015) 19027–19035.
[21] S. Garaj, W. Hubbard, A. Reina, J. Kong, D. Branton, J. Golovchenko, Nature 467 (2010) 190–193.
[22] S.C. O'Hern, C.A. Stewart, M.S. Boutilier, J.-C. Idrobo, S. Bhaviripudi, S.K. Das, J. Kong, T. Laoui, M. Atieh, R. Karnik, ACS Nano 6 (2012) 10130–10138.
[23] J. Qin, C. He, N. Zhao, Z. Wang, C. Shi, E.-Z. Liu, J. Li, ACS Nano 8 (2014) 1728–1738.
[24] V. Sahu, S. Grover, B. Tulachan, M. Sharma, G. Srivastava, M. Roy, M. Saxena, N. Sethy, K. Bhargava, D. Philip, Electrochim. Acta 160 (2015) 244–253.
[25] S. Ghosh, X. An, R. Shah, D. Rawat, B. Dave, S. Kar, S. Talapatra, J. Phys. Chem. C 116 (2012) 20688–20693.
[26] H. Seo, J.H. Chu, S.-Y. Kwon, I.C. Bang, Int. J. Heat Mass Transfer 82 (2015) 490–502.
[27] S. An, D.-Y. Kim, J.-G. Lee, H.S. Jo, M.-w. Kim, S.S. Al-Deyab, J. Choi, S.S. Yoon, Int. J. Heat Mass Transfer 98 (2016) 124–130.
[28] J. Rafiee, X. Mi, H. Gullapalli, A.V. Thomas, F. Yavari, Y. Shi, P.M. Ajayan, N.A. Koratkar, Nat. Mater. 11 (2012) 217–222.
[29] Y. Lin, G.J. Ehlert, C. Bukowsky, H.A. Sodano, ACS Appl. Mater. Interfaces 3 (2011) 2200–2203.
[30] E. Ueda, P.A. Levkin, Adv. Mater. 25 (2013) 1234–1247.
[31] T. Young, Philos. Trans. R. Soc. Lond. 95 (1805) 65–87.
[32] R.N. Wenzel, Ind. Eng. Chem. 28 (1936) 988–994.
[33] A. Cassie, Discuss. Faraday Soc. 3 (1948) 11–16.
[34] M.W. Lee, S. An, B. Joshi, S.S. Latthe, S.S. Yoon, ACS Appl. Mater. Interfaces 5 (2013) 1232–1239.
[35] A.B. Gurav, S.S. Latthe, R.S. Vhatkar, J.-G. Lee, D.-Y. Kim, J.-J. Park, S.S. Yoon, Ceram. Int. 40 (2014) 7151–7160.
[36] A.B. Gurav, Q. Xu, S.S. Latthe, R. Vhatkar, S. Liu, H. Yoon, S.S. Yoon, Ceram. Int. 41 (2015) 3017–3023.
[37] H. Yoon, H. Kim, S.S. Latthe, M.-w. Kim, S. Al-Deyab, S.S. Yoon, J. Mater. Chem. A 3 (2015) 11403–11410.
[38] D.-Y. Kim, J.-G. Lee, B.N. Joshi, S.S. Latthe, S.S. Al-Deyab, S.S. Yoon, J. Mater. Chem. A 3 (2015) 3975–3983.
[39] O. Leenaerts, B. Partoens, F. Peeters, Phys. Rev. B 79 (2009) 235440.
[40] S. Wang, Y. Zhang, N. Abidi, L. Cabrales, Langmuir 25 (2009) 11078–11081.
[41] Y.J. Shin, Y. Wang, H. Huang, G. Kalon, A.T.S. Wee, Z. Shen, C.S. Bhatia, H. Yang, Langmuir 26 (2010) 3798–3802.
[42] F. Taherian, V. Marcon, N.F. van der Vegt, F.d.r. Leroy, Langmuir 29 (2013) 1457–1465.
[43] Y. Wu, N. Aluru, J. Phys. Chem. B 117 (2013) 8802–8813.
[44] A. Ashraf, Y. Wu, M.C. Wang, N.R. Aluru, S.A. Dastgheib, S. Nam, Langmuir 30 (2014) 12827–12836.
[45] Y. Wei, C.Q. Jia, Carbon 87 (2015) 10–17.
[46] Z. Li, A. Kozbial, N. Nioradze, D. Parobek, G.J. Shenoy, M. Salim, S. Amemiya, L. Li, H. Liu, ACS Nano 10 (2016) 349–359.
[47] A. Ashraf, Y. Wu, M.C. Wang, K. Yong, T. Sun, Y. Jing, R.T. Haasch, N.R. Aluru, S. Nam, Nano Lett. 16 (2016) 4708–4712.
[48] Z. Li, Y. Wang, A. Kozbial, G. Shenoy, F. Zhou, R. McGinley, P. Ireland, B. Morganstein, A. Kunkel, S.P. Surwade, Nat. Mater. 12 (2013) 925–931.
[49] C.-Y. Lai, T.-C. Tang, C.A. Amadei, A.J. Marsden, A. Verdaguer, N. Wilson, M. Chiesa, Carbon 80 (2014) 784–792.
[50] A.I. Aria, P.R. Kidambi, R.S. Weatherup, L. Xiao, J.A. Williams, S. Hofmann, J. Phys. Chem. C 120 (2016) 2215–2224.
[51] X. Zhang, S. Wan, J. Pu, L. Wang, X. Liu, J. Mater. Chem. 21 (2011) 12251–12258.
[52] H. Sun, A. Li, X. Qin, Z. Zhu, W. Liang, J. An, P. La, W. Deng, ChemSusChem 6 (2013) 2377–2381.
[53] J. Zang, S. Ryu, N. Pugno, Q. Wang, Q. Tu, M.J. Buehler, X. Zhao, Nat. Mater. 12 (2013) 321–325.

[54] D.-a. Zha, S. Mei, Z. Wang, H. Li, Z. Shi, Z. Jin, Carbon 49 (2011) 5166–5172.
[55] E. Singh, Z. Chen, F. Houshmand, W. Ren, Y. Peles, H.M. Cheng, N. Koratkar, Small 9 (2013) 75–80.
[56] G.F. Schneider, Q. Xu, S. Hage, S. Luik, J.N. Spoor, S. Malladi, H. Zandbergen, C. Dekker, Nat. Commun. 4 (2013) 1–7.
[57] L. Karimi, M.E. Yazdanshenas, R. Khajavi, A. Rashidi, M. Mirjalili, Cellulose 21 (2014) 3813–3827.
[58] C.-J. Shih, Q.H. Wang, S. Lin, K.-C. Park, Z. Jin, M.S. Strano, D. Blankschtein, Phys. Rev. Lett. 109 (2012) 176101.
[59] C.-J. Shih, M.S. Strano, D. Blankschtein, Nat. Mater. 12 (2013) 866–869.
[60] R. Raj, S.C. Maroo, E.N. Wang, Nano Lett. 13 (2013) 1509–1515.
[61] D. Parobek, H. Liu, 2D Mater. 2 (2015) 032001.
[62] C.A. Amadei, C.-Y. Lai, M.J. Esplandiu, F. Alzina, C.D. Vecitis, A. Verdaguer, M. Chiesa, RSC Adv. 5 (2015) 39532–39538.
[63] N.N. Nguyen, S.B. Jo, S.K. Lee, D.H. Sin, B. Kang, H.H. Kim, H. Lee, K. Cho, Nano Lett. 15 (2015) 2474–2484.
[64] R. Fürstner, W. Barthlott, C. Neinhuis, P. Walzel, Langmuir 21 (2005) 956–961.
[65] A. Marmur, Langmuir 20 (2004) 3517–3519.
[66] K.K. Lau, J. Bico, K.B. Teo, M. Chhowalla, G.A. Amaratunga, W.I. Milne, G.H. McKinley, K.K. Gleason, Nano Lett. 3 (2003) 1701–1705.
[67] X. Dong, J. Chen, Y. Ma, J. Wang, M.B. Chan-Park, X. Liu, L. Wang, W. Huang, P. Chen, Chem. Commun. 48 (2012) 10660–10662.
[68] L. Feng, S. Li, H. Li, J. Zhai, Y. Song, L. Jiang, D. Zhu, Angew. Chem. 114 (2002) 1269–1271.
[69] Z.Y. Wu, C. Li, H.W. Liang, J.F. Chen, S.H. Yu, Angew Chem. 125 (2013) 2997–3001.
[70] H.B. Jiang, Y.L. Zhang, D.D. Han, H. Xia, J. Feng, Q.D. Chen, Z.R. Hong, H.B. Sun, Adv. Funct. Mater. 24 (2014) 4595–4602.
[71] Z. Lin, Y. Liu, C.-p. Wong, Langmuir 26 (2010) 16110–16114.
[72] M.A. Worsley, P.J. Pauzauskie, T.Y. Olson, J. Biener, J.H. Satcher Jr., T.F. Baumann, J. Am. Chem. Soc. 132 (2010) 14067–14069.
[73] M. Xue, H. Qiu, W. Guo, Nanotechnology 24 (2013) 505720.
[74] L. Huang, M. Zhang, C. Li, G. Shi, J. Phys. Chem. Lett. 6 (2015) 2806–2815.
[75] S. Dervin, D.D. Dionysiou, S.C. Pillai, Nanoscale 8 (2016) 15115–15131.
[76] K.A. Mahmoud, B. Mansoor, A. Mansour, M. Khraisheh, Desalination 356 (2015) 208–225.
[77] Y. You, V. Sahajwalla, M. Yoshimura, R.K. Joshi, Nanoscale 8 (2016) 117–119.
[78] H.W. Yoon, Y.H. Cho, H.B. Park, Philos. Trans. R. Soc. A 374 (2016).
[79] F. Perreault, A. Fonseca de Faria, M. Elimelech, Chem. Soc. Rev. 44 (2015) 5861–5896.
[80] D. Cohen-Tanugi, J.C. Grossman, Nano Lett. 12 (2012) 3602–3608.
[81] D. Cohen-Tanugi, J.C. Grossman, Nano Lett. 14 (2014) 6171–6178.
[82] K. Sint, B. Wang, P. Král, J. Am. Chem. Soc. 130 (2008) 16448–16449.
[83] D. Konatham, J. Yu, T.A. Ho, A. Striolo, Langmuir 29 (2013) 11884–11897.
[84] E.Y. Ang, T.Y. Ng, J. Yeo, Z. Liu, K. Geethalakshmi, Carbon 110 (2016) 350–355.
[85] J. Muscatello, F. Jaeger, O.K. Matar, E.A. Müller, ACS Appl. Mater. Interfaces 8 (2016) 12330–12336.
[86] J. Azamat, J. Phys. Chem. C 120 (2016) 23883–23891.
[87] C.J. Russo, J.A. Golovchenko, Proc. Natl. Acad. Sci. U. S. A. 109 (2012) 5953–5957.
[88] Z. Bai, L. Zhang, H. Li, L. Liu, ACS Appl. Mater. Interfaces 8 (2016) 24803–24809.
[89] S.C. O'Hern, M.S. Boutilier, J.C. Idrobo, Y. Song, J. Kong, T. Laoui, M. Atieh, R. Karnik, Nano Lett. 14 (2014) 1234–1241.
[90] D.W. Kim, J. Choi, D. Kim, H.-T. Jung, J. Mater. Chem. A 4 (2016) 17773–17781.
[91] K. Celebi, J. Buchheim, R.M. Wyss, A. Droudian, P. Gasser, I. Shorubalko, J.-I. Kye, C. Lee, H.G. Park, Science 344 (2014) 289–292.
[92] S.P. Surwade, S.N. Smirnov, I.V. Vlassiouk, R.R. Unocic, G.M. Veith, S. Dai, M. Mahurin, Nat. Nanotechnol. 10 (2015) 459–464.
[93] X.L. Xu, F.W. Lin, Y. Du, X. Zhang, J. Wu, Z.K. Xu, ACS Appl. Mater. Interfaces 8 (2016) 12588–12593.
[94] D. Cohen-Tanugi, L.C. Lin, J.C. Grossman, Nano Lett. 16 (2016) 1027–1033.
[95] H.M. Hegab, L. Zou, J. Membr. Sci. 484 (2015) 95–106.
[96] P. Sun, M. Zhu, K. Wang, M. Zhong, J. Wei, D. Wu, Z. Xu, H. Zhu, ACS Nano 7 (2013) 428–437.
[97] P. Sun, F. Zheng, M. Zhu, Z. Song, K. Wang, M. Zhong, D. Wu, R.B. Little, Z. Xu, H. Zhu, ACS Nano 8 (2014) 850–859.
[98] B. Mi, Science 343 (2014) 740–742.
[99] P. Sun, Q. Chen, X. Li, H. Liu, K. Wang, M. Zhong, J. Wei, D. Wu, R. Ma, T. Sasaki, H. Zhu, NPG Asia Mater. 7 (2015) e162.
[100] M. Hu, B. Mi, Environ. Sci. Technol. 47 (2013) 3715–3723.
[101] M. Bhadra, S. Roy, S. Mitra, Desalination 378 (2016) 37–43.
[102] B. Feng, K. Xu, A. Huang, Desalination 394 (2016) 123–130.
[103] J. Pei, X. Zhang, L. Huang, H. Jiang, X. Hu, RSC Adv. 6 (2016) 101948–101952.
[104] B.M. Ganesh, A.M. Isloor, A.F. Ismail, Desalination 313 (2013) 199–207.
[105] M.E.A. Ali, L. Wang, X. Wang, X. Feng, Desalination 386 (2016) 67–76.
[106] J. Wang, X. Gao, J. Wang, Y. Wei, Z. Li, C. Gao, ACS Appl. Mater. Interfaces 7 (2015) 4381–4389.
[107] T. Wang, J. Lu, L. Mao, Z. Wang, J. Membr. Sci. 515 (2016) 125–133.
[108] M. Sanchez-Polo, J. Rivera-Utrilla, J. Environ. Sci. Technol. 36 (2002) 3850–3854.
[109] S. Park, J.H. An, I.W. Jung, R.D. Piner, S.J. An, X.S. Li, A. Velamakanni, R.S. Ruoff, Nano Lett. 9 (2009) 1593–1597.
[110] Y. Gao, Y. Li, L. Zhang, H. Huang, J. Hu, S.M. Shah, X. Su, J. Colloid Interface Sci. 368 (2012) 540–546.
[111] H. Yan, H. Wu, K. Li, Y. Wang, X. Tao, H. Yang, A. Li, R. Cheng, ACS Appl. Mater. Interfaces 7 (2015) 6690–6697.
[112] B. Henriques, G. Goncalves, N. Emami, E. Pereira, M. Vila, P.A. Marques, J. Hazard. Mater. 301 (2016) 453–461.
[113] V. Chandra, J. Park, Y. Chun, J.W. Lee, I.-C. Hwang, K.S. Kim, ACS Nano 4 (2010) 3979–3986.
[114] T.S. Sreeprasad, S.M. Maliyekkal, K.P. Lisha, T. Pradeep, J. Hazard Mater. 186 (2010) 921–931.
[115] W. Wang, J. Yu, Q. Xiang, B. Cheng, Appl. Catal. B 119–120 (2012) 109–116.
[116] P. Gao, Z. Liu, M. Tai, D.D. Sun, W. Ng, Appl. Catal. B 138–139 (2013) 17–25.
[117] C. Xu, A. Cui, Y. Xu, X. Fu, Carbon 62 (2013) 465–471.
[118] C.P. Athanasekou, S. Morales-Torres, V. Likodimos, G.E. Romanos, L.M. Pastrana-Martinez, P. Falaras, D.D. Dionysiou, J.L. Faria, J.L. Figueiredo, A.M.T. Silva, Appl. Catal. B 158–159 (2014) 361–372.
[119] X.J. Deng, L.L. Lu, H.W. Li, F. Luo, J. Hazard. Mater. 183 (2010) 923–930.
[120] H.C. Bi, X. Xie, K.B. Yin, Y.L. Zhou, S. Wan, L.B. He, F. Xu, F. Banhart, L.T. Sun, R.S. Ruoff, Adv. Funct. Mater. 22 (2012) 4421–4425.
[121] L. Zhang, F. Zhang, X. Yang, G. Long, Y. Wu, T. Zhang, K. Leng, Y. Huang, Y. Ma, A. Yu, Y. Chen, Sci. Rep. 3 (2013) 1408.
[122] J.L. Wang, Z.X. Shi, J.C. Fan, Y. Ge, J. Yin, G.X. Hu, J. Mater. Chem. 22 (2012) 22459–22466.
[123] J.P. Zhao, W.C. Ren, H.M. Cheng, J. Mater. Chem. 22 (2012) 20197–20202.
[124] J.C. Shelton, H.R. Patil, J.M. Blakely, Surf. Sci. Rep. 43 (1974) 493–520.
[125] X. Lu, M. Yu, H. Huang, R.S. Ruoff, Nanotechnology 10 (1999) 269–272.
[126] Y. Hernadez, V. Nicolosi, M. Lotya, F.M. Blighe, Z. Sun, S. De, I.T. McGovern, B. Holland, M. Byrne, Yurii K. Gun'Ko, J.J. Boland, P. Niraj, G. Duesberg, S. Krishnamurthy, R. Goodhue, J. Hutchison, V. Scardaci, A.C. Ferrari, J.N. Coleman, Nat. Nanotechnol. 3 (2008) 563–568.
[127] A. Dato, V. Radmilovic, Z. Lee, J. Phillips, M. Frenklach, Nano Lett. 8 (2008) 2012–2016.
[128] W.S. Hummers Jr., R.E. Offeman, J. Am. Chem. Soc. 80 (1958) 1339.
[129] D.A. Dikin, S. Stankovich, E.J. Zimney, R.D. Piner, G.H.B. Dommett, G. Evmenenko, S.T. Nguyen, R. Ruoff, Nature 448 (2007) 457–460.
[130] S. Wan, F. He, J. Wu, W. Wan, Y. Gu, B. Gao, J. Hazard. Mater. 314 (2016) 32–40.
[131] G.Z. Kyzas, E.A. Deliyanni, K.A. Matis, J. Chem. Technol. Biotechnol. 89 (2014) 196–205.
[132] T.S. Sreeprasad, S.S. Gupta, S.M. Maliyekkal, T. Pradeep, J. Hazard. Mater. 246–247 (2013) 213–220.
[133] Q. Fang, B. Chen, J. Mater. Chem. A 2 (2014) 8941–8951.
[134] X. Mi, G. Huang, W. Xie, W. Wang, Y. Liu, J. Gao, Carbon 50 (2012) 4856–4864.
[135] Y. Han, Z. Xu, C. Gao, Adv. Funct. Mater. 23 (2013) 3693–3700.
[136] X. Chen, M. Qiu, H. Ding, K. Fu, Y. Fan, Nanoscale 8 (2016) 5696–5705.
[137] Y. Xu, H. Bai, G. Lu, C. Li, G. Shi, J. Am. Chem. Soc. 130 (2008) 5856–5857.
[138] S. Filice, D. D'Angelo, S. Libertino, I. Nicotera, V. Kosma, V. Privitera, S. Scalese, Carbon 82 (2015) 489–499.
[139] S. Guo, G. Zhang, Y. Guo, J.C. Yu, Carbon 60 (2013) 437–444.
[140] R.C. Pawar, D.-H. Choi, C.S. Lee, Int. J. Hydrogen Energy 40 (2015) 767–778.
[141] H. Sun, L. Cao, L. Lu, Nano Res. 4 (2011) 550–562.
[142] Y. Chen, L. Chen, H. Bai, L. Li, J. Mater. Chem. A 1 (2013) 1992–2001.
[143] A. Meidanchi, O. Akhavan, Carbon 69 (2014) 230–238.
[144] J. Liang, Y. Jiao, M. Jaroniec, S.Z. Qiao, Angew. Chem. Int. Ed. 51 (2012) 11496–11500.
[145] D. Dinda, A. Gupta, S.K. Saha, J. Mater. Chem. A 1 (2013) 11221.
[146] H. Jabeen, V. Chandra, S. Jung, J.W. Lee, K.S. Kim, S.B. Kim, Nanoscale 3 (2011) 3583–3585.
[147] Z. Sui, Q. Meng, X. Zhang, R. Ma, B. Cao, J. Mater. Chem. 22 (2012) 8767–8771.
[148] L. Hao, H. Song, L. Zhang, X. Wan, Y. Tang, Y. Lv, J. Colloid Interface Sci. 369 (2012) 381–387.
[149] L. Fan, C. Luo, M. Sun, X. Li, H. Qiu, Colloids Surf. B 103 (2013) 523–529.
[150] Y. Ren, N. Yan, Q. Wen, Z. Fan, T. Wei, M. Zhang, J. Ma, Chem. Eng. J. 175 (2011) 1–7.
[151] Z. Yang, H. Yan, H. Yang, H. Li, A. Li, R. Cheng, Water Res. 47 (2013) 3037–3046.
[152] M. Puster, J.A. Rodríguez-Manzo, A. Balan, M. Drndić, ACS Nano 7 (2013) 11283–11289.
[153] R.C. Rollings, A.T. Kuan, J.A. Golovchenko, Nat. Commun. 7 (2016) 11408.
[154] F.M. Kafiah, Z. Khan, A. Ibrahim, R. Karnik, M. Atieh, T. Laoui, Desalination 388 (2016) 29–37.
[155] S.C. O'Hern, D. Jang, S. Bose, J.C. Idrobo, Y. Song, T. Laoui, J. Kong, R. Karnik, Nano Lett. 15 (2015) 3254–3260.
[156] K. Xu, B. Feng, C. Zhou, A. Huang, Chem. Eng. Sci. 146 (2016) 159–165.
[157] T. Jiao, H. Guo, Q. Zhang, Q. Peng, Y. Tang, X. Yan, B. Li, Sci. Rep. 5 (2015) 11873.
[158] B. Liang, P. Zhang, J. Wang, J. Qu, L. Wang, X. Wang, C. Guan, K. Pan, Carbon 103 (2016) 94–100.
[159] Z. Xu, T. Wu, J. Shi, K. Teng, W. Wang, M. Ma, J. Li, X. Qian, C. Li, J. Fan, J. Membr. Sci. 520 (2016) 281–293.